International Journal of
Molecular Sciences

MDPI

Article

$Co_{0.9}Co_{0.1}S$ Nanorods with an Internal Electric Field and Photothermal Effect Synergistically for Boosting Photocatalytic H_2 Evolution

Lilei Zhang [1], Manzhou Hong [1,2], Ka Zhang [1,2], Botan Li [1], Haipeng Fang [1], Xun Feng [1,*] and Xiuchan Xiao [3]

[1] Henan Key Laboratory of Function Oriented Porous Materials, College of Chemistry and Chemical Engineering, Luoyang Normal University, Luoyang 471934, China
[2] Green Catalysis Center, College of Chemistry, Zhengzhou University, Zhengzhou 450001, China
[3] School of Materials and Environmental Engineering, Chengdu Technological University, Chengdu 611730, China
* Correspondence: fengx@lynu.edu.cn

Abstract: The paper reports a strategy to synthesize $Cd_{0.9}Co_{0.1}S$ nanorods (NRs) via a one-pot solvothermal method. Remarkably, the pencil-shaped $Cd_{0.9}Co_{0.1}S$ NRs with a large aspect ratio and good polycrystalline plane structure significantly shorten the photogenerated carrier transfer path and achieve fast separation. An appropriate amount of Co addition enhances visible light-harvesting and generates a photothermal effect to improve the surface reaction kinetics and increases the charge transfer rate. Moreover, the internal electric field facilitates the separation and transfer of carriers and effectively impedes their recombination. As a result, the optimized $Cd_{0.9}Co_{0.1}S$ NRs yield a remarkable H_2 evolution rate of 8.009 $mmol \cdot g^{-1} \cdot h^{-1}$, which is approximately 7.2 times higher than that of pristine CdS. This work improves the photocatalytic hydrogen production rate by tuning and optimizing electronic structures through element addition and using the photothermal synergistic effect.

Keywords: $Cd_{0.9}Co_{0.1}S$ nanorods; photothermal; internal electric field; pencil-shaped; photocatalytic

Citation: Zhang, L.; Hong, M.; Zhang, K.; Li, B.; Fang, H.; Feng, X.; Xiao, X. $Co_{0.9}Co_{0.1}S$ Nanorods with an Internal Electric Field and Photothermal Effect Synergistically for Boosting Photocatalytic H_2 Evolution. *Int. J. Mol. Sci.* **2022**, *23*, 9756. https://doi.org/10.3390/ijms23179756

Academic Editor: Joanna M. Kargul

Received: 10 August 2022
Accepted: 25 August 2022
Published: 28 August 2022

1. Introduction

Hydrogen is essential in the clean energy system [1–4]. Semiconductor-based photocatalytic hydrogen production is promising to alleviate increasing energy and pollution problems [5–9]. Many metal sulfide-based semiconductors have been discovered for photocatalytic hydrogen evolution. Represented by CdS, exhibiting good visible light response, narrow bandgap, and morphology controllability, it is considered one of the most promising photocatalytic materials. However, because of the severe photo-corrosion and rapid recombination of the photogenerated carrier of pure CdS, its proton-reduction efficiency is limited, resulting in poor photocatalytic performance [10–12].

Hence, several researchers have reported various strategies to elevate the photocatalytic performance of CdS-based materials. First of all, CdS with multiple shapes, such as nanoparticles [13], nanotubes [14], nanospheres [15], and nanorods [16] have been found in many studies and showed excellent photocatalytic performance. Among them, the CdS nanorods have attracted more and more attention because of their large aspect ratio and fewer defects, which can significantly shorten the radial transfer path of carriers and achieve rapid charge separation, thus exhibiting high photocatalytic hydrogen evolution performance [17,18]. In addition, several other methods have been applied, such as constructing an intrinsic built-in electric field, defect and heterostructure engineering, and co-catalyst decoration to accelerate the separation and transfer of photogenerated electron-hole pairs [19–22]. Establishing the internal electric field in semiconductors by element doping can promote the separation and transfer of photogenerated electrons, and extract

carriers, thus improving the photocatalytic efficiency. For example, the Huang group prepared a gradient P-doped CdS nanostructure via surface diffusion doping strategy [23] the Hu group reported gradient-P-doped CdS/CoP hybrid nanorods [24], and the Shangguan group explored Ni, Mo, Co-doped CdS for efficient photocatalytic hydrogen evolution from water splitting [25].

It is well known that photothermal conversion is an attractive strategy for solar light-harvesting, and the local temperature can go up in situ, which generally enhances the entropy of chemical reactions and enhances the kinetics of surface catalytic reactions to accelerate the transfer of photogenerated charges, thus increasing the photocatalytic reaction rate [26–30]. Especially in water splitting that involves a brutal thermodynamic uphill reaction, heat as an external force can effectively drive water photocatalytic hydrogen production [31]. The photothermal synergistic catalytic system that couples photochemical and thermochemical effects shows better performance than the traditional single catalytic system [32]. Therefore, using the photothermal effect to enhance CdS-based performance should be an excellent strategy.

Herein, pencil-tipped CdCoS NRs were prepared by a one-pot method, as presented in Scheme 1. In this work, we added an appropriate amount of Co into CdS NRs, which narrowed the pure CdS bandgap and significantly enhanced light-harvesting ability, achieving rapid charge separation efficiency. Meanwhile, element addition realized the construction of the internal electric field and the photothermal synergistic. Finally, the optimized $Cd_{0.9}Co_{0.1}S$ NRs photocatalyst exhibits excellent hydrogen production efficiency under visible light illumination.

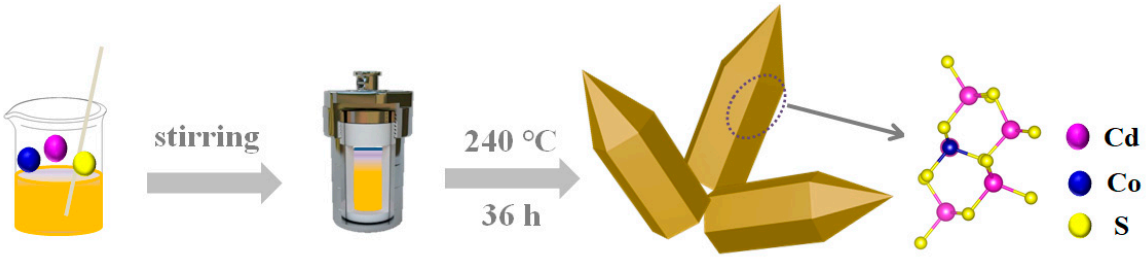

Scheme 1. Schematic illustration of the synthetic process for $Cd_{0.9}Co_{0.1}S$ nanorods structure.

2. Results and Discussion

2.1. Structure and Morphology Analysis of Photocatalysts

XRD analyzed the phase and crystal structure of the synthesized samples. As presented in Figure 1a, hexagonal phase CdS existed in all samples. The XRD pattern of pure CdS displayed several obvious peaks at 24.8, 26.5, 28.1, 36.6, 43.6, 47.8, and 51.8°, attributed to the (100), (002), (101), (102), (110), (103), and (112) planes, respectively (PFD#41-1049) [16,33]. After Co addition, the diffraction peak shifted of $Cd_{0.9}Co_{0.1}S$ NRs relative to pure CdS, and there was no obvious peak of cobalt sulfide present, indicating the change of its crystal structure. Specifically, the partially magnified XRD pattern of samples showed that the main diffraction peak positions on the CdCoS samples were slightly shifted to a higher 2θ value, which means that the lattice parameter changes [34]. The shift can be attributed to the successful incorporation of Co^{2+} into CdS because the effective ionic radius of Co^{2+} is smaller than that of Cd^{2+} [35,36]. Furthermore, the contents of Cd, Co, and S of the obtained CdCoS photocatalysts were further determined by ICP-MS. As presented in Table S1, the molar ratios of Co/Cd were 0.103, 0.228, and 0.319, corresponding to the samples $Cd_{0.9}Co_{0.1}S$, $Cd_{0.8}Co_{0.2}S$, and $Cd_{0.7}Co_{0.3}S$, respectively.

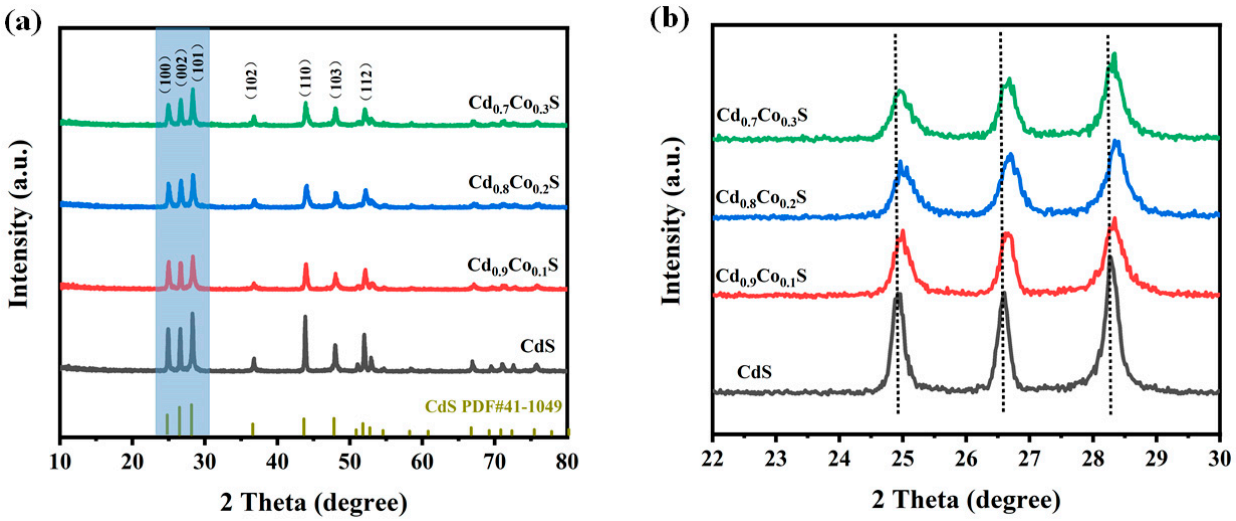

Figure 1. The XRD patterns (**a**) and partially magnified XRD patterns of pure CdS and CdCoS NRs (**b**).

The SEM and TEM images give detailed information on the microscopic structures and morphologies of $Cd_{0.9}Co_{0.1}S$ NRs. As the SEM images (Figure 2a,b) revealed, $Cd_{0.9}Co_{0.1}S$ NRs displayed a clear crystal structure with a regular polyhedral shape. The TEM images (Figure 2c–f) of $Cd_{0.9}Co_{0.1}S$ showed the nanorod-like system. It can be seen that the crystal surface is smooth after Co addition, and no obvious Co nanoparticles are found. Meanwhile, as the SAED pattern (Figure 2g) and HRTEM images (Figure 2h,i) presented, the corresponding lattice diffraction pattern of $Cd_{0.9}Co_{0.1}S$ NRs with equal lattice diffraction spacing was well matched with the (101) plane of the CdS phase. The lattice fringes with interlayer distances of 0.21 and 0.24 nm were assigned to the (110) and (102) planes [37], respectively, of pristine CdS (PDF#41-1049). In addition, elemental mapping results (Figure 2j–m) and energy dispersive spectroscopy (EDS) spectra (Figure S1) of an individual $Cd_{0.9}Co_{0.1}S$ NRs sample further confirm the existence of S, Cd, and Co elements in the photocatalyst, indicating the Co has been added successfully.

XPS studied the surface chemical state and internal elemental bond composition of samples. Figure 3a displayed the full-survey spectrum of $Cd_{0.9}Co_{0.1}S$ NRs, indicating the existence of Cd, S, C, O, and Co elements. The S 2p spectrum of $Cd_{0.9}Co_{0.1}S$ NRs in Figure 3b showed two binding energies at 160.8 and 162.0 eV, ascribed to S $2p_{3/2}$ and S $2p_{1/2}$, respectively. Simultaneously, as presented in Figure 3c, the Cd 3d spectrum of $Cd_{0.9}Co_{0.1}S$ NRs can be deconvoluted into Cd $3d_{5/2}$ (404.5 eV) and Cd $3d_{3/2}$ (411.3 eV) [31,38]. Significantly, compared with pure CdS, the two peaks of S 2p in $Cd_{0.9}Co_{0.1}S$ NRs shifted to the low binding energy region. Conversely, the characteristic peaks of Cd 3d shifted slightly to a higher position, which indicates that a fraction of Co atoms has substituted Cd sites to form the Co-S bond, resulting in the redistribution of charge around Cd and S atoms [37,39]. Moreover, the Co 2p spectrum (Figure 3d) of $Cd_{0.9}Co_{0.1}S$ NRs can be deconvoluted into four peaks. The peaks located at 781.1 and 786.1 eV and at 796.4 and 802.2 eV corresponded to Co $2p_{3/2}$ and Co $2p_{1/2}$, respectively [40,41]. Such results further indicated that Co had been successfully added into the composites.

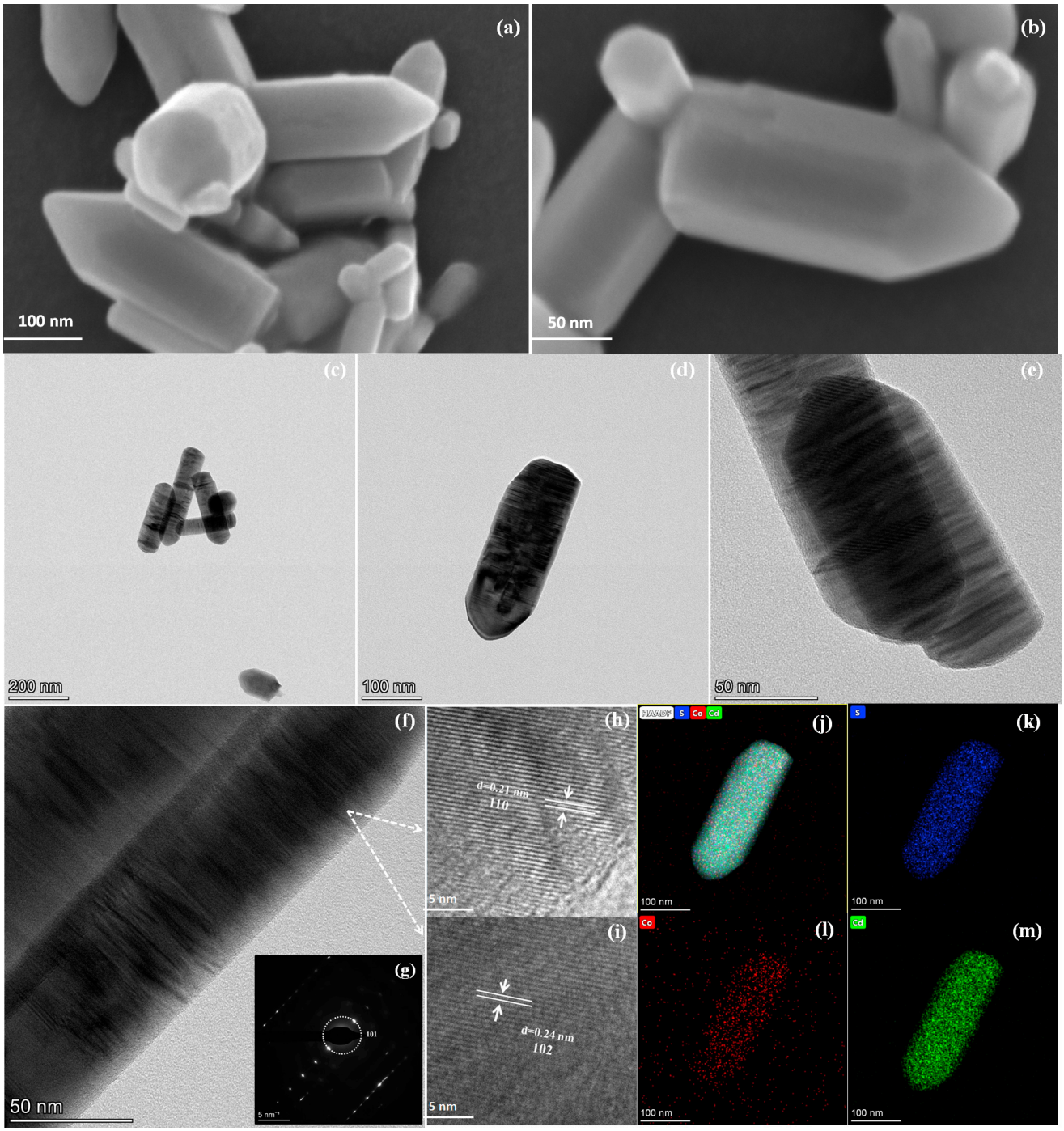

Figure 2. SEM images (**a**,**b**) and TEM images (**c**–**f**), SAED pattern (**g**), HRTEM images (**h**,**i**), and elemental mappings (**j**–**m**) of the $Cd_{0.9}Co_{0.1}S$ NRs.

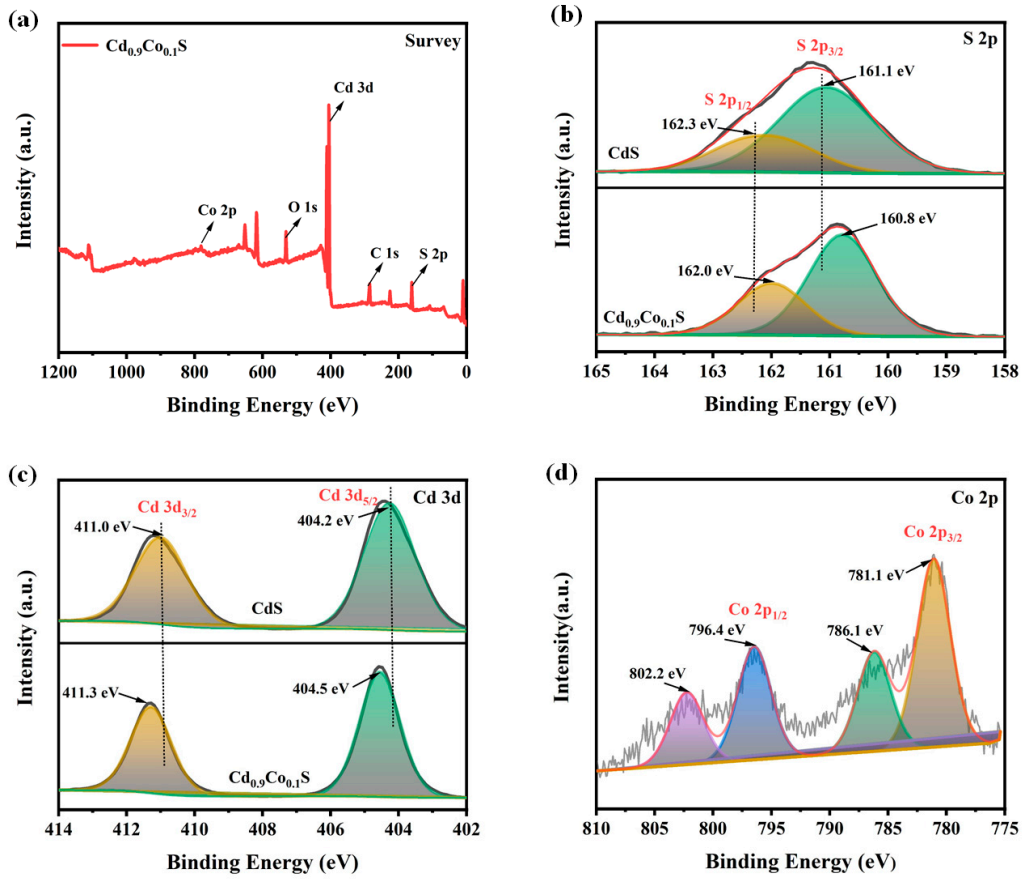

Figure 3. XPS survey spectra of $Cd_{0.9}Co_{0.1}S$ NRs (**a**), and high-resolution XPS spectra of: S 2p (**b**), Cd 3d (**c**) in the CdS and $Cd_{0.9}Co_{0.1}S$ NRs, and Co 2p (**d**) in the $Cd_{0.9}Co_{0.1}S$ NRs.

2.2. Photocatalytic H_2 Evolution Performance

Photocatalytic H_2 evolution performance was evaluated in the prepared samples. As demonstrated in Figure 4a,b, pure CdS exhibited the lowest H_2 evolution rate of 1.12 mmol·g^{-1}·h^{-1}, gradually declining in the reaction. After Co addition, the H_2 evolution rate of all CdCoS NRs was significantly enhanced. In particular, the hydrogen evolution rate of $Cd_{0.9}Co_{0.1}S$ NRs reached the highest value of 8.009 mmol·g^{-1}·h^{-1} (Video S1), which is about 7.2 times that of pure CdS. It surpassed most of the other CdS-based photocatalysts previously reported (Table S2). With the increase of Co addition, the hydrogen evolution rate gradually reduced because excessive added elements may become new carrier recombination centers, which hindered the proton-reduction process [42]. Therefore, the appropriate amount of Co addition is essential to enhance photocatalytic activity significantly. The apparent quantum efficiency (AQE) is an important measure of photocatalytic hydrogen production performance, equal to twice the number of evolved H_2 molecules divided by the number of incident photons. The AQE of $Cd_{0.9}Co_{0.1}S$ NRs under different monochromatic light irradiations were calculated. As shown in Figure 4c, it was 1.77, 9.60, and 3.80% at 365, 420, and 700 nm, respectively, which indicated that the photocatalyst had a modest utilization efficiency of light. It confirmed the crucial role of the photothermal synergistic effect in significantly improving the H_2 generation performance of $Cd_{0.9}Co_{0.1}S$ NRs.

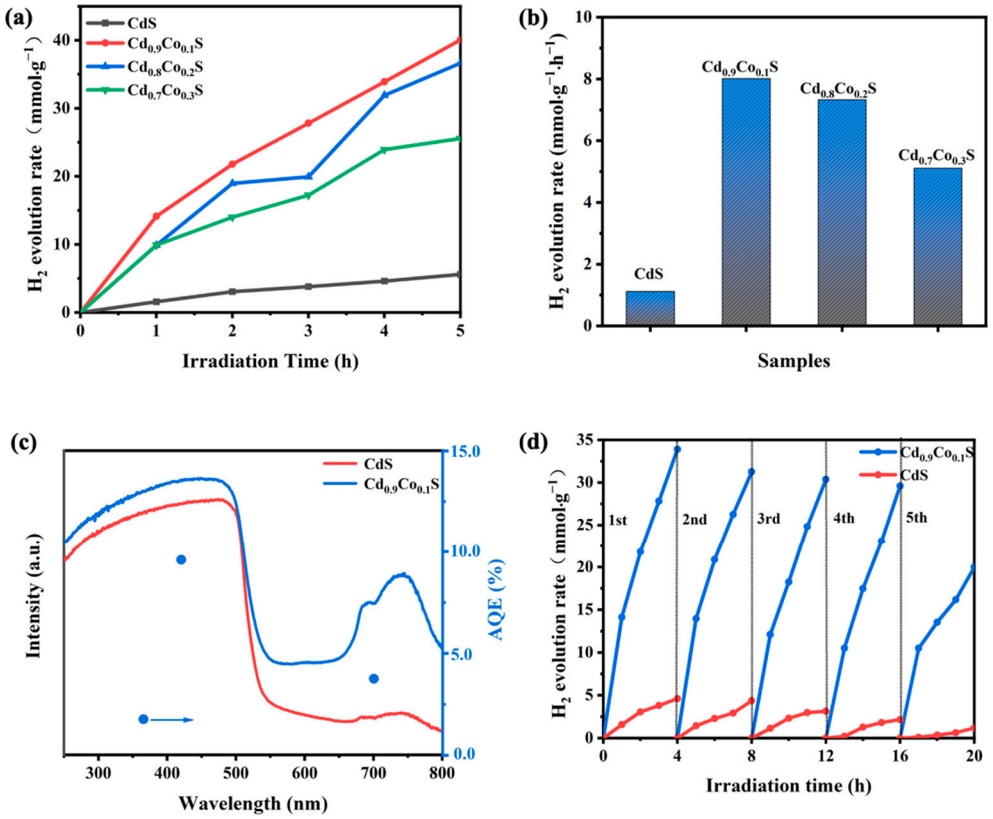

Figure 4. Time-dependent photocatalytic H_2 evolution (**a**) and H_2 evolution rates for all samples (**b**). Apparent quantum efficiency (AQE) and the UV–vis absorption spectrum of $Cd_{0.9}Co_{0.1}S$ NRs (**c**). The AQE equals twice the number of evolved H_2 molecules divided by the number of incident photons under light irradiation with specific wavelengths (365, 420, and 700 nm). Cyclic tests of photocatalytic H_2 evolution for pure CdS and $Cd_{0.9}Co_{0.1}S$ (**d**).

Moreover, the photocatalytic H_2 production stability of $Cd_{0.9}Co_{0.1}S$ NRs was evaluated through a 20 h cyclic photocatalytic test, with a total of five cycles, each cycle of 4 h, and the results were shown in Figure 4d. In the first three cycles, the hydrogen production of the sample remained unchanged. In the 5th cycle reaction, the hydrogen evolution rate of $Cd_{0.9}Co_{0.1}S$ NRs has decreased. However, it was still significantly higher than pure CdS, possibly due to the loss of photocatalyst quality and sacrificial agent in the reaction process. Therefore, we supplemented the sacrificial agent and photocatalyst after five cycles of stability testing. The results (Figure S4a) showed that the hydrogen production performance increased after the supplement but decreased compared to the initial examination.

It is known that the photo-corrosion of CdS is one of the main reasons affecting its performance. When the CdS is photo-corroded, the Cd^{2+} will be dispersed into the dispersion solution. To clarify the degree of photo-corrosion of the photocatalyst during the reaction, the Cd^{2+} concentration in the reaction solution of each run was monitored by ICP. As displayed in Figure S4b, the Cd^{2+} concentration in pure CdS increases rapidly with the progress of the reaction. Meanwhile, it can be seen from the XPS spectra (Figure S5) after the cyclic response that there is a small amount of S^0 in the S 2p spectrum of pure CdS, which was attributed to the oxidation of divalent sulfur, indicating that obvious photo-corrosion occurred in pure CdS during the reaction process.

In comparison, the Cd^{2+} concentration in $Cd_{0.9}Co_{0.1}S$ NRs has increased but was much lower than pure CdS. This result showed that $Cd_{0.9}Co_{0.1}S$ NRs have a little photo-corrosion under long-time illumination, leading to its performance decline. However, compared with pure CdS, Co addition reduced photo-corrosion and improved the stability of the

photocatalyst. Furthermore, the SEM images (Figure S2) and XRD spectra (Figure S6) of $Cd_{0.9}Co_{0.1}S$ NRs showed that the morphology and phase of the photocatalyst did not change after cyclic tests, indicating that the photocatalyst had good stability.

2.3. Photothermal Effect

Temperature is one of the influential critical factors in photocatalytic reaction, and an appropriate temperature increase is conducive to photo-catalytic response [43,44]. To verify the photothermal synergistic effect of the photocatalytic, the surface temperature changes of pristine CdS and $Cd_{0.9}Co_{0.1}S$ NRs under visible light irradiation were tracked in situ. As illustrated in Figure 5a,b, the surface temperatures of $Cd_{0.9}Co_{0.1}S$ NRs increased rapidly in 300 s and reached 50.1 °C from 25.0 °C, which was higher than that of pristine CdS. Compared with pure CdS, the $Cd_{0.9}Co_{0.1}S$ NRs exhibited better photothermal properties, indicating that the Co-S bond formed after proper Co addition played a crucial role in the photothermal effect of photocatalytic reaction [45,46]. In the photothermal phenomenon, as the conversion from light to heat, high temperature can generally accelerate the transfer of charge carriers and surface reaction kinetics, thus improving the photocatalytic performance [47–49]. To investigate the effect of temperature on photocatalytic H_2 generation, the photocatalytic H_2 evolution rate of $Cd_{0.9}Co_{0.1}S$ NRs at different temperatures was measured. As shown in Figure 5c, the H_2 evolution rate declined sharply with the decrease in reaction temperature, indicating that the excellent photothermal effect of $Cd_{0.9}Co_{0.1}S$ NRs played an essential role in its better photocatalytic performance.

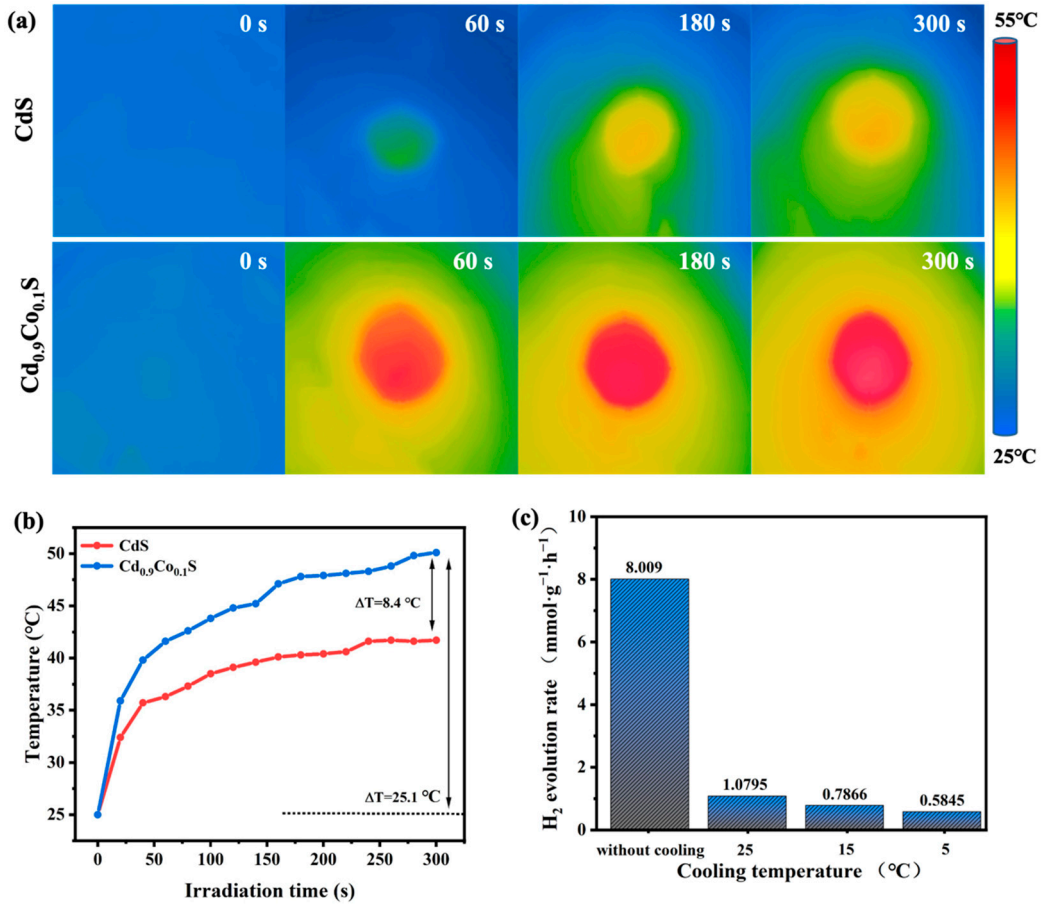

Figure 5. Infrared thermography photos (**a**), the time-dependent temperature of the pure CdS and $Cd_{0.9}Co_{0.1}S$ NRs under visible light (**b**), and H_2 evolution rates of $Cd_{0.9}Co_{0.1}S$ NRs without and with cooling the reaction solutions (**c**).

2.4. Optical Property and Band Structure

The UV-vis absorption spectra of the samples were measured to analyze their light-absorption properties. As displayed in Figure 6a, the pure CdS has an inherent bandgap (Eg) adsorption with a band edge of about 520 nm. Compared with pure CdS, with the increase of Co addition, the CdCoS NRs exhibited better light absorption capacity in the wavelength range of 230–520 nm, and all CdS-based photocatalysts had a redshift. Notably, CdCoS NRs showed an obvious tail absorbance in the field of 550–800 nm. It speculates that the tail absorbance in the 550–800 nm field is mainly caused by the vibration of Co atoms in the lattice. As the band gap of $Cd_{0.7}Co_{0.3}S$ NRs became wider (Figure 6b), the absorbance decreased slightly. However, it was still significantly higher than pure CdS, demonstrating that Co addition can enhance the light-harvesting ability of the photocatalysts. Meanwhile, the samples showed a strong absorption peak around 740 nm, which may enable them to have a higher photothermal conversion efficiency.

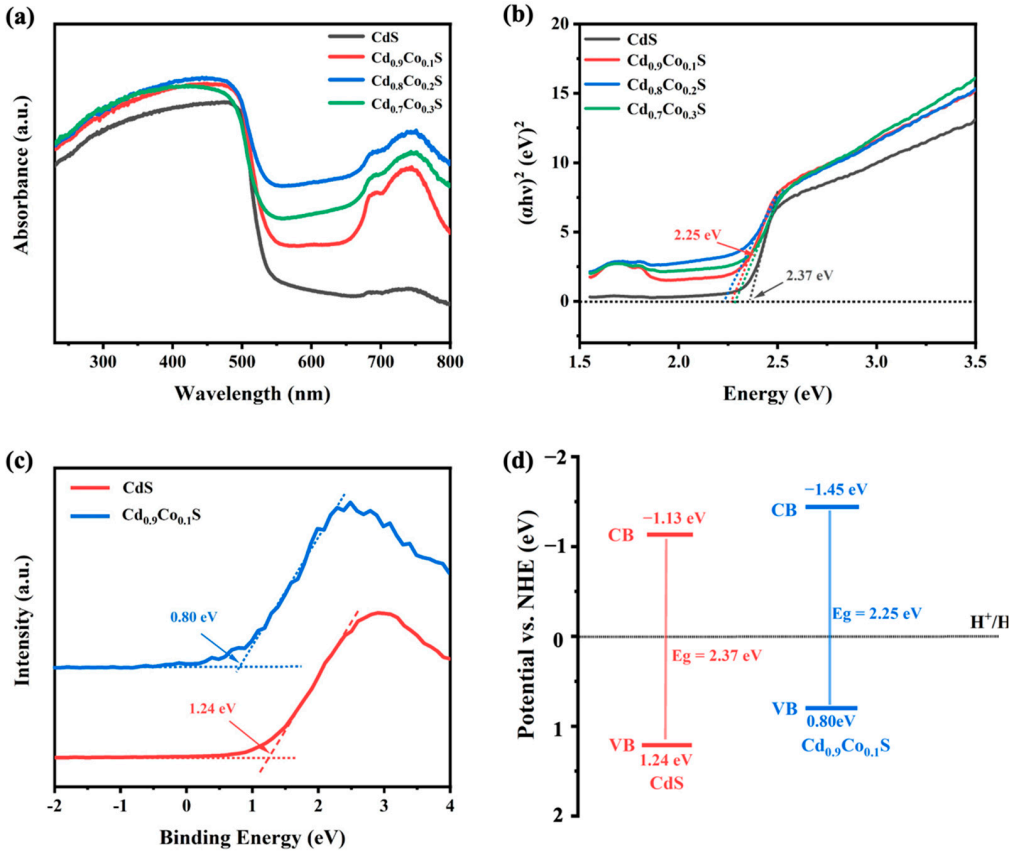

Figure 6. UV–vis diffuse reflectance spectra (**a**), corresponding Tauc plots (**b**), XPS valence band spectra (**c**), and Schematic band structures of pure CdS and $Cd_{0.9}Co_{0.1}S$ NRs (**d**).

The appropriate band structure of the catalyst is essential to charge-oriented transfer, with a suitable bandgap, the suitable conduction band (CB) and valance band (VB) edge potentials [50]. As displayed in Figure 6b, the bandgap energy of CdS and $Cd_{0.9}Co_{0.1}S$ NRs calculated based on the Kubelka–Munk method from the Tauc plots were 2.37 and 2.25 eV, respectively. As presented in Figure 6c, the VB value of pure CdS and $Cd_{0.9}Co_{0.1}S$ NRs were 1.24 and 0.80 eV, respectively. The VB value is the energy of the intersection point obtained by extending the straight part near 0 eV and extending the horizontal part less than 0 eV. Moreover, the Mott-Schottky method measured the E_{fb} (flat-band potential) of pristine CdS and $Cd_{0.9}Co_{0.1}S$ NRs. As shown in Figure S3a,b, the Mott–Schottky plots of CdS and $Cd_{0.9}Co_{0.1}S$ NRs showed a positive slope, indicating that semiconductors have n-type characteristics [51], and the flat band potentials (E_{fb}) of CdS and $Cd_{0.9}Co_{0.1}S$ NRs were approximately −1.17 and −1.49 V (vs. SCE), respectively. The measured potentials can

be converted to the standard hydrogen electrode (NHE) scale by the Nernst equation [52] (Equation (1)):

$$E_{(NHE)} = E_{(SCE)} + 0.24 \quad (1)$$

By calculation, the E_{fb} of CdS and $Cd_{0.9}Co_{0.1}S$ NRs were −0.93 and −1.25 V (vs. NHE), respectively. Theoretically, the conduction band position of n-type semiconductors is −0.2 V negative than flat band potential [39,53]. So, the conduction band positions (E_{CB}) of CdS and $Cd_{0.9}Co_{0.1}S$ NRs were −1.13 and −1.45 eV, respectively. The formula $E_g = E_{VB} - E_{CB}$ shows that the calculated results match well with the test results. Therefore, the band energy alignment of CdS and $Cd_{0.9}Co_{0.1}S$ NRs can be determined (Figure 6d). It can be seen that Co addition can narrow the bandgap, and the $Cd_{0.9}Co_{0.1}S$ NRs have a more negative CB, indicating that it has a higher reduction power and is more beneficial to solar hydrogen production [50,54].

2.5. Separation and Transfer of Charge Carriers

A series of photoelectron-chemical measurements were carried out to discuss further the reasons for the excellent photocatalytic performance of $Cd_{0.9}Co_{0.1}S$ NRs. Generally speaking, the photoluminescence (PL) peak's low intensity indicates the charge carriers' low recombination efficiency [55]. It can be seen from Figure 7a that the pure CdS showed the strongest PL peak at about 390 nm, which is owing to the rapid recombination of electrons and holes. After Co addition, the P.L. signal of the sample was significantly reduced, which indicated that Co addition could effectively accelerate the charge separation and reduce its recombination efficiency. However, with the increase of Co addition, too much Co formed new active sites, further reducing the recombination of photogenerated carriers, so the sample $Cd_{0.7}Co_{0.3}S$ NRs had the lowest PL signal. In addition, the time-resolved photoluminescence (TRPL) spectra showed the average lifetime of charge carriers of samples under irradiation, and the results are illustrated in Figures 7b and S7. The average lifetimes of carriers were 0.71, 1.25, 0.96, and 0.89 ns for pure CdS, $Cd_{0.9}Co_{0.1}S$, $Cd_{0.8}Co_{0.2}S$, and $Cd_{0.7}Co_{0.3}S$ NRs, respectively. The $Cd_{0.9}Co_{0.1}S$ NRs exhibited the longest carrier lifetime, indicating that the Co addition in $Cd_{0.9}Co_{0.1}S$ can significantly improve electron-hole pairs separation efficiency [56], and a long lifetime of the carrier means more opportunities to participate in the hydrogen evolution reactions [57]. The above results indicated that Co addition could effectively capture electron-hole pairs and thus effectively prevent their recombination.

Transient photocurrent tests examined the efficiency of separating the electron-hole pairs. As presented in Figure 7c, $Cd_{0.9}Co_{0.1}S$ NRs showed the highest photocurrent density among all samples, indicating the highest charge separation efficiency. Compared with pristine CdS, an appropriate amount of Co addition can accelerate the separation and transfer of charge carriers. Furthermore, electronic transmission capacity is a significant factor for catalysts, and electrochemical impedance spectroscopy (EIS) was utilized to study the resistance of the electrode/electrolyte interface of different catalysts during the photocatalytic process [58]. As can be seen clearly from Figure 7d, the radius of the Nyquist circle of the $Cd_{0.9}Co_{0.1}S$ NRs was significantly smaller than that of other samples, indicating that it has the minor charge transfer resistance to ensure the fastest charge transfer rate. In summary, the above photochemical characterization results confirm that the $Cd_{0.9}Co_{0.1}S$ NRs can improve charge separation, enhance charge transfer and prolong charge lifetime, thus significantly enhancing the photocatalytic performance of hydrogen evolution.

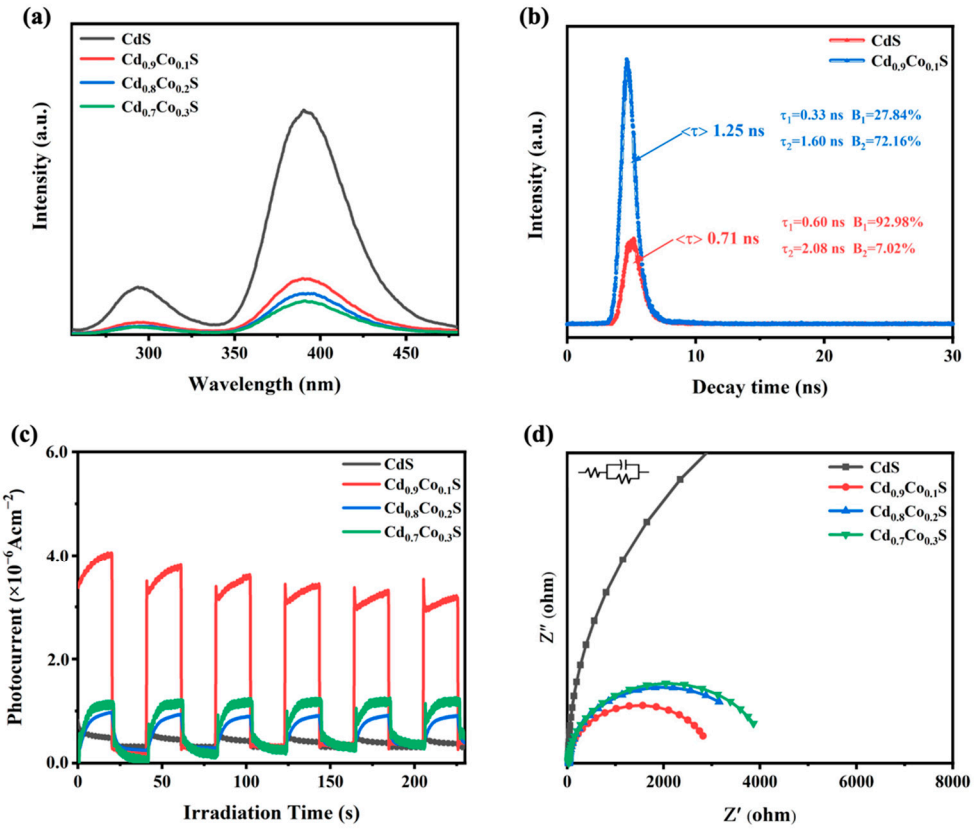

Figure 7. PL spectra (**a**), TRPL decay spectra (**b**), photocurrent responses (**c**), and EIS plots (**d**) of as-prepared samples.

2.6. Photocatalytic Mechanism

To deeply understand the electronic regulation effect of Co addition strategy in CdS, density functional theory (DFT) calculations were performed. As shown in Figure 8a, the structure model of $Cd_{0.9}Co_{0.1}S$ NRs was constructed. After Co addition, the local electronic structure of $Cd_{0.9}Co_{0.1}S$ NRs was changed. Figure 8b,c showed the optimal configuration and different charge densities, and the charge of $Cd_{0.9}Co_{0.1}S$ NRs also depleted or accumulated in other regions. Specifically, Co atoms caused the loss of surrounding electrons. Meanwhile, the electron density of S atoms increased (the brown and green isosurfaces depict electron accumulation and electron depletion, respectively). Therefore, an internal electric field was built in $Cd_{0.9}Co_{0.1}S$ NRs, which boosted the separation of electrons and holes, and inhibited its recombination [25].

Based on the frontier molecular orbital theory, the region near the Fermi level is essential for photocatalysis [59,60]. As shown in Figure 8c, with Co addition, the bandgap of $Cd_{0.9}Co_{0.1}S$ NRs 2.05 eV was narrower than that of pure CdS 2.12 eV (Figure S8), which helps the absorption of visible light. The simulation results were consistent with the experimental value. The valence band maximum (VBM) and conduction band minimum (CBM) of $Cd_{0.9}Co_{0.1}S$ NRs are located at the same Γ point, indicating that the sample is a direct bandgap semiconductor [49,61]. It is noteworthy that metallic materials can generate electrons and holes through inter-band and intra-band transitions [62]. Therefore, the sample can produce electron-hole pairs more easily under visible light irradiation. Furthermore, the density of states (DOS) and partial density of states (PDOS) of $Cd_{0.9}Co_{0.1}S$ NRs were displayed in Figure 8d. The partial PDOS of $Cd_{0.9}Co_{0.1}S$ NRs was decomposed according to the contribution of different elements. As a result, the VBM is principally contributed by S orbital, and the CBM is mainly contributed by the hybridization of S, Cd, and Co orbitals, thus forming the Co-S bond. After absorbing photons, the Co-S bonds can act as a "bridge" for charge transfer, thus inhibiting the carrier recombination [38].

Figure 8e shows the phonon spectrum of $Cd_{0.9}Co_{0.1}S$ NRs and the contribution of Co and Cd atoms. It can be seen that the Co addition generates new lattice vibration frequencies, which will lead to solar light absorptions. It is consistent with the characterization results of UV-Vis. In addition, the high-frequency vibration is mainly due to the contribution of Co atoms, which will lead to a strong thermal effect, thus increasing the emission of hydrogen and the reaction rate of hydrogen production.

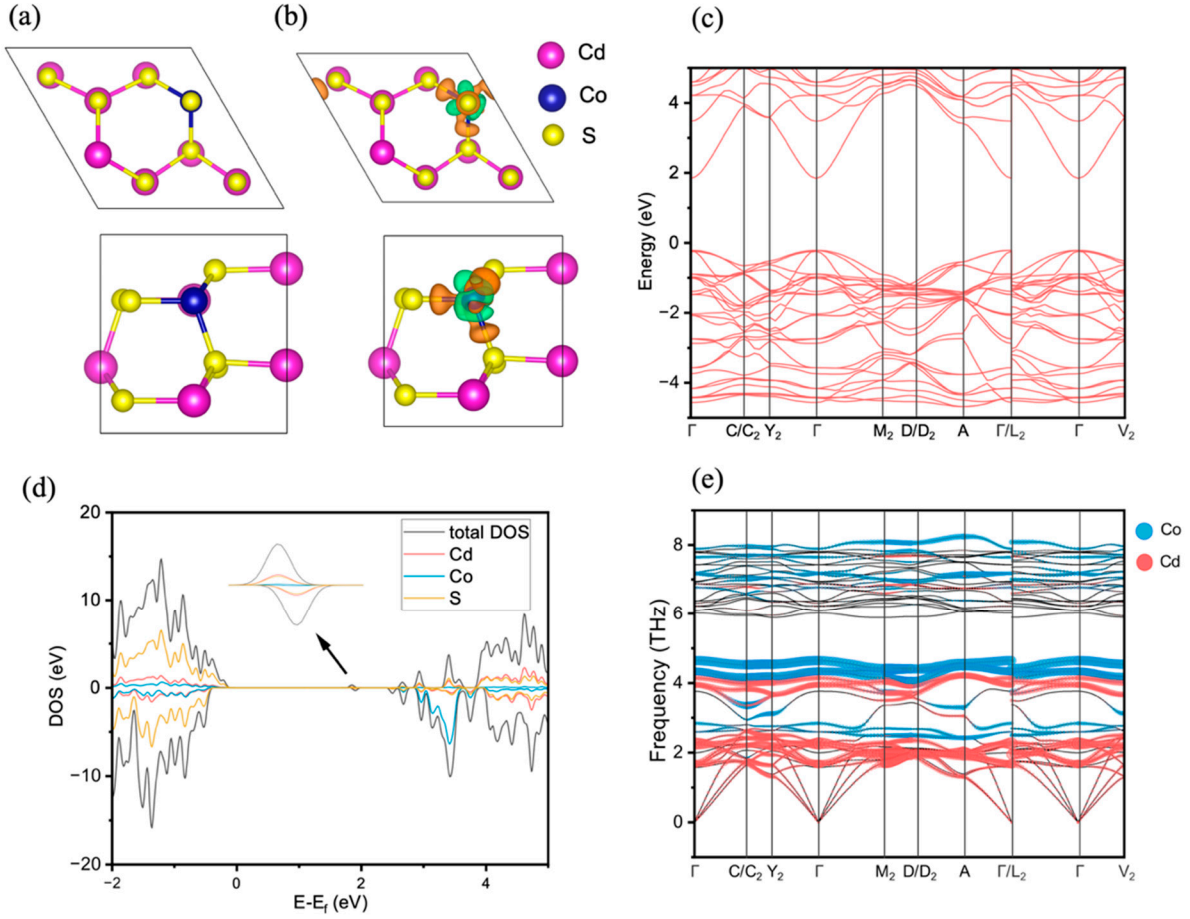

Figure 8. DFT calculation: side views of structural model (**a**), and Charge density differences of $Cd_{0.9}Co_{0.1}S$ NRs (**b**) brown (gain electron), green (lose electron), Electronic band structure (**c**), and Total and projected density of states for $Cd_{0.9}Co_{0.1}S$ NRs (**d**) (spin-up is upper half, spin-down is lower half), and Phonon spectra for $Cd_{0.9}Co_{0.1}S$ NRs (**e**).

Based on the above analysis, the possible mechanism for the charge carrier excitation and migration processes of $Cd_{0.9}Co_{0.1}S$ NRs photocatalyst can be depicted in Scheme 2. Firstly, Co^{2+} partially filled with d orbital generates electron donor levels in the bandgap when it partially enters the CdS lattice, thus narrowing the bandgap. Under visible light irradiation, the narrower bandgap of $Cd_{0.9}Co_{0.1}S$ NRs is more conducive to light-harvesting and generating electrons and holes. Then, Co addition caused spontaneous electron density redistribution in $Cd_{0.9}Co_{0}.1S$ NRs. In detail, Co atoms caused the loss of surrounding electrons, and the electron density of S atoms increased.

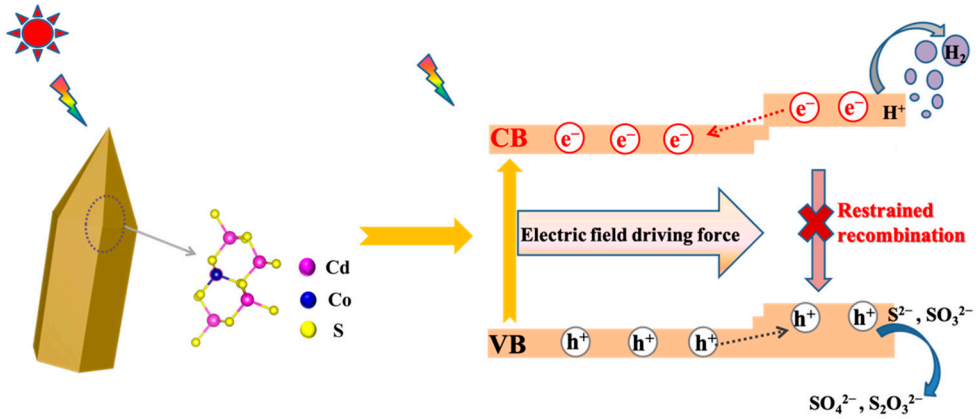

Scheme 2. Diagram of the proposed photocatalytic mechanism of $Cd_{0.9}Co_{0.1}S$ NRs under visible light irradiation.

Meanwhile, the E_{VB} and E_{fb} of $Cd_{0.9}Co_{0.1}S$ NRs rose, and the band gap decreased. After illumination, due to the generation and migration of carriers, E_{fb} equilibrates and band bends because of the generation and migration of carriers, thus forming an internal electric field. The formed internal electric field can significantly inhibit the recombination of electron-hole pairs and prolong the lifetime of the charge carrier. In addition, the extra energy is converted from chemical energy to thermal energy through photothermal reaction under light irradiation, thereby accelerating the migration rate of carriers in $Cd_{0.9}Co_{0.1}S$ NRs. Eventually, the electrons gathered in the CB of $Cd_{0.9}Co_{0.1}S$ NRs encounter H^+ and release H_2. The holes accumulated in the VB can obtain enough power to oxidate the sacrificial agent.

3. Materials and Methods

3.1. Characterization

The morphologies were determined by SEM (Tecnai G20) and TEM (FEI Talos F200S). XRD patterns were analyzed using a Bruker D8 Advance X-ray diffractometer. The element content of the samples was measured by ICP-MS (PerkinElmer NexION 300X). XPS spectra were conducted using an ESCALAB 250xi spectrometer. FT-IR spectra were recorded on Nicolet 6700 infrared spectrometer. UV-vis diffuse reflectance spectra were recorded on a UH-4150 spectrophotometer, and the bandgap was calculated using the absorption data. Photoluminescence emission spectra were recorded on the Hitachi F-7000 Fluorescence spectrophotometer. The fluorescence lifetime of the sample was measured and exponentially fitted by Edinburgh FLS1000 Photoluminescence Spectrometer. The FLIR monitored infrared thermal images of the sample.

3.2. Synthesis of CdCoS NRs

CdCoS NRs were synthesized via a one-pot solvothermal method. In a typical synthesis, firstly, 9 mmol cadmium acetate ($Cd(CH_3COO)_2{\cdot}2H_2O$), 12.5 mmol thioacetamide, and 1 mmol cobalt nitrate ($Co(NO_3)_2{\cdot}6H_2O$) were dissolved in 15 mL of ethylenediamine and 15 mL of deionized water. Then, the mixture solution was transferred into a 50 mL Teflon-lined stainless-steel autoclave and stirred at room temperature for 1 h. Finally, the mixture solution was maintained at 240 °C for 36 h. After suction filtration and vacuum drying, the obtained sample was simply denoted as $Cd_{0.9}Co_{0.1}S$ (Cd/Co = 9:1). Meanwhile, under the same experimental conditions, the molar ratio of $Cd(CH_3COO)_2{\cdot}2H_2O$ and $Co(NO_3)_2{\cdot}6H_2O$ was changed to 8:2 and 7:3 respectively, and the obtained samples were named as $Cd_{0.8}Co_{0.2}S$ (Cd/Co = 8:2) and $Cd_{0.7}Co_{0.3}S$ (Cd/Co = 7:3), respectively.

3.3. Photocatalytic H_2 Evolution

The photocatalytic H_2 evolution experiment was carried out in a top-irradiated quartz reactor (Labsolar-6A, Perfectlight) with a circulating water system. Typically, 80 mg of

photocatalysts were dispersed by ultrasound in a 100 mL Na_2SO_3 (0.35 M) and Na_2S (0.25 M) mixture [63]. Before performing the photocatalytic experiments, the reaction vessel was purged with N_2 and evacuated for at least 30 min to remove dissolved air. The 300 W Xe-lamp was used as a light source. GC-9790 (Ar as the carrier) gas chromatograph tested the separated hydrogen gas with a thermal conductive detector. Under the same conditions, the blank experiment revealed no appreciable H_2 evolution without photocatalysts.

3.4. The Apparent Quantum Efficiency Analysis

The apparent quantum efficiency (AQE) was performed under the same reaction conditions except using various band-pass filters (365, 420, and 700 nm) to obtain the monochromatic light, and the following equation calculated the value of AQE:

$$AQE = \frac{2 \times the\ number\ of\ evolved\ H_2\ molecules}{the\ number\ of\ incident\ photons} \times 100\%$$

Details on experimental materials, characterization, photocatalytic H_2 evolution, and photoelectrochemical measurements are shown in the Supporting Information.

3.5. Theoretical Calculation

The Vienna Ab-initio Simulation Package (VASP) [64–66] based on the projector augmented wave (PAW) method was carried out for the first principle calculations. All material configurations were geometrically optimized by relaxing the ions and lattice with the Perdew–Burke–Ernzerhof (PBE) parameterization and Monkhorst–Pack k-meshes of $6 \times 6 \times 8$ until the maximum residual ionic force is less than 10^{-4} eV. The cutoff energy of the plane-wave was set to 400 eV. The accurate band structures and density of occupied states were obtained using Heyd–Scuseria–Ernzerhof (HSE06) hybrid density functional [67]. The second interatomic force constants and phono structure were obtained using the Phonopy package [68] with $2 \times 2 \times 2$ supercells. The Vaspkit software package [69] was adopted to analyze the band structures and density of occupied states, and the Vesta software [70] was used to visualize the calculation results.

4. Conclusions

In summary, through a one-pot strategy, we successfully prepared $Cd_{0.9}Co_{0.1}S$ NRs with excellent H_2 production performance (8.009 $mmol \cdot g^{-1} \cdot h^{-1}$). The pencil-shaped $Cd_{0.9}Co_{0.1}S$ NRs can shorten the radial transfer path of electrons and realize rapid charge separation. Meanwhile, the Co addition significantly enhanced visible light-harvesting, reduced the bandgap, and generated a photothermal synergy to improve the charge transfer rate and surface reaction kinetics. Moreover, the internal electric field accelerates the separation and migration of charge carriers and effectively inhibits the recombination of electrons and holes. This work may provide an optimal platform to design and construct stable nano photocatalysts for solar energy conversion.

Supplementary Materials: The following supporting information can be downloaded at: https://www.mdpi.com/article/10.3390/ijms23179756/s1. References [71–81] are cited in the supplementary materials.

Author Contributions: L.Z.: Conceptualization, Validation, Methodology, Writing—review & editing. M.H.: Data curation, Investigation, Writing—original draft. K.Z.: Visualization, Investigation. B.L.: Investigation, Software, Validation. H.F.: Data curation. X.F.: Supervision, Project administration, Resources. X.X.: Software; Investigation; Visualization. All authors have read and agreed to the published version of the manuscript.

Funding: This research was funded by the program for science & technology innovation team in universities of Henan province grant number [21IRTSTHN004] and the national natural science foundation of China grant number [U1804131] and the key scientific research projects of universities in Henan province grant number [22A430032].

Institutional Review Board Statement: Not applicable.

Informed Consent Statement: Not applicable.

Data Availability Statement: Not applicable.

Acknowledgments: This work was supported by the Program for Science & Technology Innovation Team in Universities of Henan Province (No. 21IRTSTHN004). The National Natural Science Foundation of China (No. U1804131), and Key scientific research projects of universities in Henan Province (No. 22A430032).

Conflicts of Interest: The authors declare no conflict of interest.

References

1. Schultz, D.M.; Yoon, T.P. Solar synthesis: Prospects in visible light photocatalysis. *Science* **2014**, *343*, 1239176. [CrossRef] [PubMed]
2. Chu, S.; Majumdar, A. Opportunities and challenges for a sustainable energy future. *Nature* **2012**, *488*, 294–303. [CrossRef] [PubMed]
3. Uddin, N.; Zhang, H.; Du, Y.; Jia, G.; Wang, S.; Yin, Z. Structural-Phase Catalytic Redox Reactions in Energy and Environmental Applications. *Adv. Mater.* **2020**, *32*, e1905739. [CrossRef] [PubMed]
4. Wang, Z.; Li, C.; Domen, K. Recent developments in heterogeneous photocatalysts for solar-driven overall water splitting. *Chem. Soc. Rev.* **2019**, *48*, 2109–2125. [CrossRef]
5. Zhao, G.; Sun, Y.; Zhou, W.; Wang, X.; Chang, K.; Liu, G.; Liu, H.; Kako, T.; Ye, J. Superior Photocatalytic H2 Production with Cocatalytic Co/Ni Species Anchored on Sulfide Semiconductor. *Adv. Mater.* **2017**, *29*, 1703258. [CrossRef]
6. Chava, R.K.; Do, J.; Kang, M. Strategy for improving the visible photocatalytic H2 evolution activity of 2D graphitic carbon nitride nanosheets through the modification with metal and metal oxide nanocomponents. *Appl. Catal. B-Environ.* **2019**, *248*, 538–551. [CrossRef]
7. Wang, Y.; Zhang, J.; Balogun, M.S.; Tong, Y.; Huang, Y. Oxygen vacancy–based metal oxides photoanodes in photoelectrochemical water splitting. *Mater. Today Sustain.* **2022**, *18*, 100118. [CrossRef]
8. Wang, Y.; Chen, D.; Zhang, J.; Balogun, M.-S.; Wang, P.; Tong, Y.; Huang, Y. Charge Relays via Dual Carbon-Actions on Nanostructured BiVO4 for High Performance Photoelectrochemical Water Splitting. *Adv. Funct. Mater.* **2022**, *32*, 2112738. [CrossRef]
9. Huang, Y.; Long, B.; Tang, M.; Rui, Z.; Balogun, M.-S.; Tong, Y.; Ji, H. Bifunctional catalytic material: An ultrastable and high-performance surface defect CeO2 nanosheets for formaldehyde thermal oxidation and photocatalytic oxidation. *Appl. Catal. B-Environ.* **2016**, *181*, 779–787. [CrossRef]
10. Zhou, P.; Zhang, Q.; Xu, Z.; Shang, Q.; Wang, L.; Chao, Y.; Li, Y.; Chen, H.; Lv, F.; Zhang, Q.; et al. Atomically Dispersed Co-P3 on CdS Nanorods with Electron-Rich Feature Boosts Photocatalysis. *Adv. Mater.* **2020**, *32*, e1904249. [CrossRef]
11. Tian, L.; Min, S.; Wang, F. Integrating noble-metal-free metallic vanadium carbide cocatalyst with CdS for efficient visible-light-driven photocatalytic H2 evolution. *Appl. Catal. B-Environ.* **2019**, *259*, 118029. [CrossRef]
12. Zhang, P.; Luan, D.; Lou, X.W.D. Fabrication of CdS Frame-in-Cage Particles for Efficient Photocatalytic Hydrogen Generation under Visible-Light Irradiation. *Adv. Mater.* **2020**, *32*, e2004561. [CrossRef] [PubMed]
13. Xia, Y.; Cheng, B.; Fan, J.; Yu, J.; Liu, G. Unraveling Photoexcited Charge Transfer Pathway and Process of CdS/Graphene Nanoribbon Composites toward Visible-Light Photocatalytic Hydrogen Evolution. *Small* **2019**, *15*, e1902459. [CrossRef] [PubMed]
14. Wang, R.; Chen, S.; Ng, Y.H.; Gao, Q.; Yang, S.; Zhang, S.; Peng, F.; Fang, Y.; Zhang, S. ZnO/CdS/PbS nanotube arrays with multi-heterojunctions for efficient visible-light-driven photoelectrochemical hydrogen evolution. *Chem. Eng. J.* **2019**, *362*, 658–666. [CrossRef]
15. Feng, R.; Wan, K.; Sui, X.; Zhao, N.; Li, H.; Lei, W.; Yu, J.; Liu, X.; Shi, X.; Zhai, M.; et al. Anchoring single Pt atoms and black phosphorene dual co-catalysts on CdS nanospheres to boost visible-light photocatalytic H_2 evolution. *Nano Today* **2021**, *37*, 101080. [CrossRef]
16. Wang, B.; Chen, C.; Jiang, Y.; Ni, P.; Zhang, C.; Yang, Y.; Lu, Y.; Liu, P. Rational designing 0D/1D Z-scheme heterojunction on CdS nanorods for efficient visible-light-driven photocatalytic H2 evolution. *Chem. Eng. J.* **2021**, *412*, 128690. [CrossRef]
17. Zhang, M.; Hu, Q.; Ma, K.; Ding, Y.; Li, C. Pyroelectric effect in CdS nanorods decorated with a molecular Co-catalyst for hydrogen evolution. *Nano Energy* **2020**, *73*, 104801. [CrossRef]
18. Lu, X.; Chen, W.; Yao, Y.; Wen, X.; Hart, J.N.; Tsounis, C.; Ying Toe, C.; Scott, J.; Ng, Y.H. Photogenerated charge dynamics of CdS nanorods with spatially distributed MoS2 for photocatalytic hydrogen generation. *Chem. Eng. J.* **2021**, *420*, 127709. [CrossRef]
19. Ai, Z.; Zhang, K.; Chang, B.; Shao, Y.; Zhang, L.; Wu, Y.; Hao, X. Construction of CdS@Ti_3C_2@CoO hierarchical tandem p-n heterojunction for boosting photocatalytic hydrogen production in pure water. *Chem. Eng. J.* **2020**, *383*, 123130. [CrossRef]
20. Yin, X.-L.; Li, L.-L.; Liu, M.-L.; Li, D.-C.; Shang, L.; Dou, J.-M. MoSx/CdS nano-heterostructures accurately constructed on the defects of CdS for efficient photocatalytic H2 evolution under visible light irradiation. *Chem. Eng. J.* **2019**, *370*, 305–313. [CrossRef]
21. Zhang, T.; Meng, F.; Cheng, Y.; Dewangan, N.; Ho, G.W.; Kawi, S. Z-scheme transition metal bridge of Co9S8/Cd/CdS tubular heterostructure for enhanced photocatalytic hydrogen evolution. *Appl. Catal. B-Environ.* **2021**, *286*, 119853. [CrossRef]

22. Shi, J.-W.; Sun, D.; Zou, Y.; Ma, D.; He, C.; Ji, X.; Niu, C. Trap-level-tunable Se doped CdS quantum dots with excellent hydrogen evolution performance without co-catalyst. *Chem. Eng. J.* **2019**, *364*, 11–19. [CrossRef]
23. Huang, H.; Dai, B.; Wang, W.; Lu, C.; Kou, J.; Ni, Y.; Wang, L.; Xu, Z. Oriented Built-in Electric Field Introduced by Surface Gradient Diffusion Doping for Enhanced Photocatalytic H2 Evolution in CdS Nanorods. *Nano Lett.* **2017**, *17*, 3803–3808. [CrossRef] [PubMed]
24. Guo, C.; Li, L.; Chen, F.; Ning, J.; Zhong, Y.; Hu, Y. One-step phosphorization preparation of gradient-P-doped CdS/CoP hybrid nanorods having multiple channel charge separation for photocatalytic reduction of water. *J. Colloid Interface Sci.* **2021**, *596*, 431–441. [CrossRef]
25. Yan, J.; Wei, Z.; Xu, M.; Jiang, Z.; Shangguan, W. Polyoxometalate Template-Based Synthetic Strategy to Prepare Ni, Mo Co-Doped CdS for Efficient Photocatalytic Hydrogen Evolution from Water Splitting. *Catalysts* **2020**, *10*, 1478. [CrossRef]
26. Guo, S.; Li, X.; Li, J.; Wei, B. Boosting photocatalytic hydrogen production from water by photothermally induced biphase systems. *Nat. Commun.* **2021**, *12*, 1343. [CrossRef]
27. Jiang, H.; Xing, Z.; Zhao, T.; Yang, Z.; Wang, K.; Li, Z.; Yang, S.; Xie, L.; Zhou, W. Plasmon Ag nanoparticle/Bi2S3 ultrathin nanobelt/oxygen-doped flower-like MoS2 nanosphere ternary heterojunctions for promoting charge separation and enhancing solar-driven photothermal and photocatalytic performances. *Appl. Catal. B-Environ.* **2020**, *274*, 118947. [CrossRef]
28. Li, Y.; Xue, J.; Shen, Q.; Jia, S.; Li, Q.; Li, Y.; Liu, X.; Jia, H. Construction of a ternary spatial junction in yolk–shell nanoreactor for efficient photo-thermal catalytic hydrogen generation. *Chem. Eng. J.* **2021**, *423*, 130188. [CrossRef]
29. Guo, M.; Zhao, T.; Xing, Z.; Qiu, Y.; Pan, K.; Li, Z.; Yang, S.; Zhou, W. Hollow Octahedral Cu_2-xS/CdS/Bi_2S_3 p-n-p Type Tandem Heterojunctions for Efficient Photothermal Effect and Robust Visible-Light-Driven Photocatalytic Performance. *ACS Appl. Mater. Interfaces* **2020**, *12*, 40328–40338. [CrossRef]
30. Huang, Y.; Lu, Y.; Lin, Y.; Mao, Y.; Ouyang, G.; Liu, H.; Zhang, S.; Tong, Y. Cerium-based hybrid nanorods for synergetic photo-thermocatalytic degradation of organic pollutants. *J. Mater. Chem. A* **2018**, *6*, 24740–24747. [CrossRef]
31. Lv, X.; Li, X.; Yang, C.; Ding, X.; Zhang, Y.; Zheng, Y.-Z.; Li, S.; Sun, X.; Tao, X. Large-Size, Porous, Ultrathin NiCoP Nanosheets for Efficient Electro/Photocatalytic Water Splitting. *Adv. Funct. Mater.* **2020**, *30*, 1910830. [CrossRef]
32. Ghoussoub, M.; Xia, M.; Duchesne, P.N.; Segal, D.; Ozin, G. Principles of photothermal gas-phase heterogeneous CO_2 catalysis. *Energ. Environ. Sci.* **2019**, *12*, 1122–1142. [CrossRef]
33. Luo, M.; Liu, Y.; Hu, J.; Liu, H.; Li, J. One-pot synthesis of CdS and Ni-doped CdS hollow spheres with enhanced photocatalytic activity and durability. *ACS Appl. Mater. Interfaces* **2012**, *4*, 1813–1821. [PubMed]
34. Deka, K.; Kalita, M.P.C. Structural phase controlled transition metal (Fe, Co, Ni, Mn) doping in CdS nanocrystals and their optical, magnetic and photocatalytic properties. *J. Alloys Comp.* **2018**, *757*, 209–220. [CrossRef]
35. Zhang, B.; Chen, C.; Liu, J.; Qiao, W.; Zhao, J.; Yang, J.; Yu, Y.; Chen, S.; Qin, Y. Simultaneous Ni nanoparticles decoration and Ni doping of CdS nanorods for synergistically promoting photocatalytic H2 evolution. *Appl. Surf. Sci.* **2020**, *508*, 144869. [CrossRef]
36. Wang, S.; Wang, Y.; Zhang, S.L.; Zang, S.Q.; Lou, X.W.D. Supporting Ultrathin ZnIn2S4 Nanosheets on Co/N-Doped Graphitic Carbon Nanocages for Efficient Photocatalytic H2 Generation. *Adv. Mater.* **2019**, *31*, e1903404. [CrossRef]
37. Ning, X.; Wu, Y.; Ma, X.; Zhang, Z.; Gao, R.; Chen, J.; Shan, D.; Lu, X. A Novel Charge Transfer Channel to Simultaneously Enhance Photocatalytic Water Splitting Activity and Stability of CdS. *Adv. Func. Mater.* **2019**, *29*, 1902992. [CrossRef]
38. Li, N.; Ding, Y.; Wu, J.; Zhao, Z.; Li, X.; Zheng, Y.Z.; Huang, M.; Tao, X. Efficient, Full Spectrum-Driven H2 Evolution Z-Scheme Co_2P/CdS Photocatalysts with Co-S Bonds. *ACS Appl. Mater. Interfaces* **2019**, *11*, 22297–22306. [CrossRef]
39. Li, S.; Wang, L.; Li, Y.; Zhang, L.; Wang, A.; Xiao, N.; Gao, Y.; Li, N.; Song, W.; Ge, L.; et al. Novel photocatalyst incorporating Ni-Co layered double hydroxides with P-doped CdS for enhancing photocatalytic activity towards hydrogen evolution. *Appl. Catal. B-Environ.* **2019**, *254*, 145–155. [CrossRef]
40. Wu, D.; Wei, Y.; Ren, X.; Ji, X.; Liu, Y.; Guo, X.; Liu, Z.; Asiri, A.M.; Wei, Q.; Sun, X. $Co(OH)_2$ Nanoparticle-Encapsulating Conductive Nanowires Array: Room-Temperature Electrochemical Preparation for High-Performance Water Oxidation Electrocatalysis. *Adv. Mater.* **2018**, *30*, 1705366. [CrossRef]
41. Qiu, B.; Zhu, Q.; Du, M.; Fan, L.; Xing, M.; Zhang, J. Efficient Solar Light Harvesting CdS/Co9 S8 Hollow Cubes for Z-Scheme Photocatalytic Water Splitting. *Angew. Chem. Int. Ed. Engl.* **2017**, *56*, 2684–2688. [CrossRef] [PubMed]
42. Chen, W.; Wang, Y.; Liu, M.; Gao, L.; Mao, L.; Fan, Z.; Shangguan, W. In situ photodeposition of cobalt on CdS nanorod for promoting photocatalytic hydrogen production under visible light irradiation. *Appl. Surf. Sci.* **2018**, *444*, 485–490. [CrossRef]
43. Li, X.; Zhang, H.; Liu, Y.; Duan, X.; Xu, X.; Liu, S.; Sun, H.; Wang, S. Synergy of NiO quantum dots and temperature on enhanced photocatalytic and thermophoto hydrogen evolution. *Chem. Eng. J.* **2020**, *390*, 124634. [CrossRef]
44. Li, X.; Lin, J.; Li, J.; Zhang, H.; Duan, X.; Sun, H.; Huang, Y.; Fang, Y.; Wang, S. Temperature-Induced Variations in Photocatalyst Properties and Photocatalytic Hydrogen Evolution: Differences in UV, Visible, and Infrared Radiation. *ACS Sustain. Chem. Eng.* **2021**, *9*, 7277–7285. [CrossRef]
45. Jin, B.; Li, Y.; Wang, J.; Meng, F.; Cao, S.; He, B.; Jia, S.; Wang, Y.; Li, Z.; Liu, X. Promoting Oxygen Evolution Reaction of Co-Based Catalysts (Co3O4, CoS, CoP, and CoN) through Photothermal Effect. *Small* **2019**, *15*, 1903847. [CrossRef]
46. Zhao, L.; Yang, Q.; Guo, W.; Liu, H.; Ma, T.; Qu, F. $Co_{2.67}S_4$-Based Photothermal Membrane with High Mechanical Properties for Efficient Solar Water Evaporation and Photothermal Antibacterial Applications. *ACS Appl. Mater. Interfaces* **2019**, *11*, 20820–20827. [CrossRef]

47. Wang, M.; Zhang, G.; Guan, Z.; Yang, J.; Li, Q. Spatially Separating Redox Centers and Photothermal Effect Synergistically Boosting the Photocatalytic Hydrogen Evolution of ZnIn2 S4 Nanosheets. *Small* **2021**, *17*, e2006952. [CrossRef]
48. Lu, L.; Xu, X.; An, K.; Wang, Y.; Shi, F.-N. Coordination Polymer Derived NiS@g-C_3N_4 Composite Photocatalyst for Sulfur Vacancy and Photothermal Effect Synergistic Enhanced H2 Production. *ACS Sustain. Chem. Eng.* **2018**, *6*, 11869–11876. [CrossRef]
49. Wang, K.; Xing, Z.; Meng, D.; Zhang, S.; Li, Z.; Pan, K.; Zhou, W. Hollow $MoSe_2$@Bi_2S_3/CdS Core-Shell Nanostructure as Dual Z-Scheme Heterojunctions with Enhanced Full Spectrum Photocatalytic-Photothermal Performance. *Appl. Catal. B-Environ.* **2021**, *281*, 119482. [CrossRef]
50. Wang, G.; Zhang, T.; Yu, W.; Si, R.; Liu, Y.; Zhao, Z. Modulating Location of Single Copper Atoms in Polymeric Carbon Nitride for Enhanced Photoredox Catalysis. *ACS Catalysis* **2020**, *10*, 5715–5722. [CrossRef]
51. Xiao, R.; Zhao, C.; Zou, Z.; Chen, Z.; Tian, L.; Xu, H.; Tang, H.; Liu, Q.; Lin, Z.; Yang, X. In situ fabrication of 1D CdS nanorod/2D Ti3C2 MXene nanosheet Schottky heterojunction toward enhanced photocatalytic hydrogen evolution. *Appl. Catal. B-Environ.* **2020**, *268*, 118382. [CrossRef]
52. Yang, X.; Qian, F.; Wang, Y.; Li, M.; Lu, J.; Li, Y.; Bao, M. Constructing a novel ternary composite (C16H33(CH3)3N)4W10O32/g-C3N4/rGO with enhanced visible-light-driven photocatalytic activity for degradation of dyes and phenol. *Appl. Catal. B-Environ.* **2017**, *200*, 283–296. [CrossRef]
53. Li, X.; Yu, J.; Low, J.; Fang, Y.; Xiao, J.; Chen, X. Engineering heterogeneous semiconductors for solar water splitting. *J. Mater. Chem. A* **2015**, *3*, 2485–2534. [CrossRef]
54. Han, M.; Lu, S.; Qi, F.; Zhu, S.; Sun, H.; Yang, B. Carbon Dots–Implanted Graphitic Carbon Nitride Nanosheets for Photocatalysis: Simultaneously Manipulating Carrier Transport in Inter- and Intralayers. *Solar RRL* **2020**, *4*, 2070041. [CrossRef]
55. Cao, S.; Li, H.; Tong, T.; Chen, H.-C.; Yu, A.; Yu, J.; Chen, H.M. Single-Atom Engineering of Directional Charge Transfer Channels and Active Sites for Photocatalytic Hydrogen Evolution. *Adv. Funct. Mater.* **2018**, *28*, 1870224. [CrossRef]
56. Yang, W.; Zhang, L.; Xie, J.; Zhang, X.; Liu, Q.; Yao, T.; Wei, S.; Zhang, Q.; Xie, Y. Enhanced Photoexcited Carrier Separation in Oxygen-Doped ZnIn2 S4 Nanosheets for Hydrogen Evolution. *Angew. Chem. Int. Ed. Engl.* **2016**, *55*, 6716–6720. [CrossRef] [PubMed]
57. Li, Z.; Hou, J.; Zhang, B.; Cao, S.; Wu, Y.; Gao, Z.; Nie, X.; Sun, L. Two-dimensional Janus heterostructures for superior Z-scheme photocatalytic water splitting. *Nano Energy* **2019**, *59*, 537–544. [CrossRef]
58. Zhang, W.; Peng, Q.; Shi, L.; Yao, Q.; Wang, X.; Yu, A.; Chen, Z.; Fu, Y. Merging Single-Atom-Dispersed Iron and Graphitic Carbon Nitride to a Joint Electronic System for High-Efficiency Photocatalytic Hydrogen Evolution. *Small* **2019**, *15*, e1905166. [CrossRef]
59. Zhang, L.; Zhang, J.; Xia, Y.; Xun, M.; Chen, H.; Liu, X.; Yin, X. Metal-Free Carbon Quantum Dots Implant Graphitic Carbon Nitride: Enhanced Photocatalytic Dye Wastewater Purification with Simultaneous Hydrogen Production. *Int. J. Mol. Sci.* **2020**, *21*, 1052. [CrossRef]
60. Zhang, L.; Zhang, J.; Qi, M.; Guo, X.; Feng, X. First-Principles Investigation of Single-Atom Ni–g-C3N4 as an Efficient Catalyst for Direct Reduction of NO with CO. *Energ. Fuel.* **2020**, *34*, 12792–12799. [CrossRef]
61. Shao, B.; Liu, X.; Liu, Z.; Zeng, G.; Liang, Q.; Liang, C.; Cheng, Y.; Zhang, W.; Liu, Y.; Gong, S. A novel double Z-scheme photocatalyst Ag_3PO_4/Bi_2S_3/Bi_2O_3 with enhanced visible-light photocatalytic performance for antibiotic degradation. *Chem. Eng. J.* **2019**, *368*, 730–745. [CrossRef]
62. Xu, J.; Ju, Z.; Zhang, W.; Pan, Y.; Zhu, J.; Mao, J.; Zheng, X.; Fu, H.; Yuan, M.; Chen, H.; et al. Efficient Infrared-Light-Driven CO_2 Reduction Over Ultrathin Metallic Ni-doped CoS_2 Nanosheets. *Angew. Chem. Int. Ed. Engl.* **2021**, *60*, 8705–8709. [CrossRef]
63. Kumaravel, V.; Imam, M.D.; Badreldin, A.; Chava, R.K.; Do, J.Y.; Kang, M.; Abdel-Wahab, A. Photocatalytic Hydrogen Production: Role of Sacrificial Reagents on the Activity of Oxide, Carbon, and Sulfide Catalysts. *Catalysts* **2019**, *9*, 276. [CrossRef]
64. Kresse, G.; Furthmüller, J. Efficiency of ab-initio total energy calculations for metals and semiconductors using a plane-wave basis set. *Comput. Mater. Sci.* **1996**, *6*, 15–50. [CrossRef]
65. Kresse, G.; Furthmüller, J. Efficient iterative schemes for ab initio total-energy calculations using a plane-wave basis set. *Phys. Rev. B* **1996**, *54*, 11169–11186. [CrossRef]
66. Kresse, G.; Hafner, J. Ab initio molecular dynamics for liquid metals. *Phys. Rev. B* **1993**, *47*, 558–561. [CrossRef]
67. Heyd, J.; Scuseria, G.E.; Ernzerhof, M. Hybrid functionals based on a screened Coulomb potential. *J. Chem. Phys.* **2003**, *118*, 8207–8215. [CrossRef]
68. Togo, A.; Tanaka, I. First principles phonon calculations in materials science. *Scr. Mater.* **2015**, *108*, 1–5. [CrossRef]
69. Wang, V.; Xu, N.; Liu, J.-C.; Tang, G.; Geng, W.-T. VASPKIT: A user-friendly interface facilitating high-throughput computing and analysis using VASP code. *Comput. Phys. Commun.* **2021**, *267*, 108033. [CrossRef]
70. Momma, K.; Izumi, F. VESTA 3 for three-dimensional visualization of crystal, volumetric and morphology data. *J. Appl. Crystallogr.* **2011**, *44*, 1272–1276. [CrossRef]
71. Li, X.; Lv, X.; Li, N.; Wu, J.; Zheng, Y.-Z.; Tao, X. One-step hydrothermal synthesis of high-percentage 1T-phase MoS_2 quantum dots for remarkably enhanced visible-light-driven photocatalytic H_2 evolution. *Appl. Catal. B-Environ.* **2019**, *243*, 76–85. [CrossRef]
72. Zhao, Q.; Yao, W.; Huang, C.; Wu, Q.; Xu, Q. Effective and Durable Co Single Atomic Cocatalysts for Photocatalytic Hydrogen Production. *ACS Appl. Mater. Interfaces* **2017**, *9*, 42734–42741. [CrossRef] [PubMed]
73. Liu, Y.; Zeng, C.; Ai, L.; Jiang, J. Boosting charge transfer and hydrogen evolution performance of CdS nanocrystals hybridized with MoS2 nanosheets under visible light irradiation. *Appl. Surf. Sci.* **2019**, *484*, 692–700. [CrossRef]

74. Liu, Y.; Niu, H.; Gu, W.; Cai, X.; Mao, B.; Li, D.; Shi, W. In-situ construction of hierarchical CdS/MoS_2 microboxes for enhanced visible-light photocatalytic H2 production. *Chem. Eng. J.* **2018**, *339*, 117–124. [CrossRef]
75. Li, H.; Pan, J.; Zhao, W.; Li, C. The 2D nickel-molybdenum bimetals sulfide synergistic modified hollow cubic CdS towards enhanced photocatalytic water splitting hydrogen production. *Appl. Surf. Sci.* **2019**, *497*, 143769. [CrossRef]
76. Guo, J.; Liang, Y.; Liu, L.; Hu, J.; Wang, H.; An, W.; Cui, W. Core-shell structure of sulphur vacancies-CdS@CuS: Enhanced photocatalytic hydrogen generation activity based on photoinduced interfacial charge transfer. *J. Colloid Interface Sci.* **2021**, *600*, 138–149. [CrossRef] [PubMed]
77. Ruan, D.; Fujitsuka, M.; Majima, T. Exfoliated Mo2C nanosheets hybridized on CdS with fast electron transfer for efficient photocatalytic H2 production under visible light irradiation. *Appl. Catal. B-Environ.* **2020**, *264*, 118541. [CrossRef]
78. Qin, Y.; Li, H.; Lu, J.; Meng, F.; Ma, C.; Yan, Y.; Meng, M. Nitrogen-doped hydrogenated TiO2 modified with CdS nanorods with enhanced optical absorption, charge separation and photocatalytic hydrogen evolution. *Chem. Eng. J.* **2020**, *384*, 123275. [CrossRef]
79. Zhu, Y.; Chen, J.; Shao, L.; Xia, X.; Liu, Y.; Wang, L. Oriented facet heterojunctions on CdS nanowires with high photoactivity and photostability for water splitting. *Appl. Catal. B-Environ.* **2020**, *268*, 118744. [CrossRef]
80. Yin, X.L.; Li, L.L.; Li, D.C.; Wei, D.H.; Hu, C.C.; Dou, J.M. Room temperature synthesis of CdS/SrTiO3 nanodots-on-nanocubes for efficient photocatalytic H2 evolution from water. *J. Colloid Interface Sci.* **2019**, *536*, 694–700. [CrossRef]
81. Luo, X.; Ke, Y.; Yu, L.; Wang, Y.; Homewood, K.P.; Chen, X.; Gao, Y. Tandem CdS/TiO_2(B) nanosheet photocatalysts for enhanced H_2 evolution. *Appl. Surf. Sci.* **2020**, *515*, 145970. [CrossRef]